

## 2 In situ calibration of the single photoelectron charge 3 response of the IceCube photomultipliers

---

**IceCube author list to be inserted... E-mail:** `analyses@icecube.wisc.edu`

ABSTRACT: This technical report outlines the in situ calibration of the single photoelectron charge distributions for each of the Hamamatsu Photonics R7081-02 photomultipliers in the IceCube Neutrino Observatory. We discuss the single photoelectron identification procedure, how we extract the single photoelectron charge distribution using a deconvolution the multi-photoelectron charge distribution, and examine various correlations between the shape of the single photoelectron charge distribution and various hardware components. The time dependence of the charge distributions is also investigated.

Definitions (this will be removed in the final draft):

1. Charge: WaveDeform fits the waveform with an SPE pulses template. The integral of the fitted pulse, divided by the load resistance, divided by the gain, is the reported measured *charge* of the pulse. It is reported in units of a single electron.
2. PE: The unit of charge. This represents the charge relative to one electron.
3. 1PE: The HV on each DOM is set such that the gain on the PMT is  $10^7$ . It is determined to be at the proper gain ( $10^7$ ), when the Gaussian mean of the fitted charge distribution is at 1PE.
4. Photoelectron: The physical electron emitted from the photocathode.
5. SPE: (Single Photoelectron) A single physical electron emitted from the photocathode.
6. MPE: (Multiple Photoelectron): multiple electrons emitted from the photocathode, charges may have been combined.
7. Charge distribution: The distribution of the measured charges. This will include both SPE and MPE events.
8. Single Photoelectron Charge distribution: The hypothetical charge distribution generated by observing a pure sample of single photoelectron.
9. SPE Template: The functional form that is used to fit the charge distribution.

5 **KEYWORDS:** IceCube, single photoelectron, charge distribution, PMT.

---

## 7 Contents

8	<b>1. Introduction</b>	<b>1</b>
9	1.1 Single photoelectron charge distributions	3
10	1.2 IceCube datasets and software definitions	5
11	<b>2. Extracting the SPE templates</b>	<b>6</b>
12	2.1 Single photoelectron pulse selection	6
13	2.2 Characterizing the low-charge region	7
14	2.3 Fitting procedure	8
15	2.4 SPE template fit results	9
16	<b>3. Discussion</b>	<b>10</b>
17	3.1 Correlations between fit parameters and DOM hardware differences	10
18	3.2 Quantifying observable changes when modifying the PMT charge distributions	12
19	3.2.1 Model comparison	13
20	3.3 SPE templates in simulation	14
21	3.4 SPE templates for calibration	14
22	<b>4. Conclusion</b>	<b>15</b>

---

## 24 1. Introduction

25 The IceCube Neutrino Observatory [1, 2] is a cubic-kilometer sized array of 5,160 photomultiplier tubes (PMTs) buried in the Antarctic ice sheet designed to observe high-energy neutrinos  
 26 interacting with the ice [3]. In 2011, the IceCube collaboration completed the installation of 86  
 27 vertical *strings* of PMT modules; 8 of which were arranged in a more densely arranged array for  
 28 the DeepCore detector [4] and the remaining for the main IceCube detector. Each string in the  
 29 detector contains 60 digital optical modules (DOMs), that contain a single PMT each, as well as  
 30 all required electronics [5]. The DOMs extend from 1450 m to 2450 m below the surface of the ice  
 31 sheet and are spaced 17 m apart in the IceCube detector, and 7 m apart in the DeepCore detector.  
 32

33 Each DOM consists of a 0.5" thick spherical glass pressure vessel that houses a single down-  
 34 facing 10" R7081-02 PMT from Hamamatsu Photonics [6]. The PMT is specified for wavelengths  
 35 ranging from 300 nm to 650 nm, with peak quantum efficiency of 25% near 390 nm. Each PMT is  
 36 coupled to the glass housing with optical gel and is surrounded by a wire mesh of  $\mu$ -metal to reduce  
 37 the effect of the ambient Earth's magnetic field. Then glass housing is transparent to wavelengths  
 38 350 nm and above [7].

39 IceCube has also deployed 399 DOMs with Hamamatsu R7081-02MOD PMTs, which, having  
 40 a peak quantum efficiency of 34% near 390 nm (36% higher efficiency than the standard DOMs),

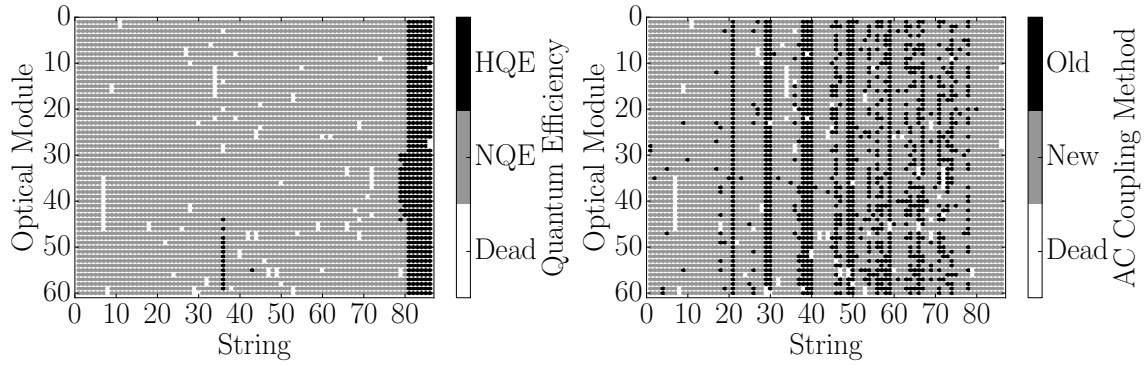


**Figure 1.** Left: Mapping showing the HQE DOMs (black) and standard normal quantum efficiency (NQE) DOMs (gray). Right: The version of AC coupling, old toroids (black) and new toroids (gray). These figures also show the location of the dead DOMs in white.

41 are classified as high-quantum efficiency (HQE) DOMs [4]. These DOMs are primarily located in  
 42 DeepCore, however there are a few located on strings 36 and 43 as well, as shown in the left side  
 43 of Fig. 1.

44 The R7081-02 and R7081-02MOD PMTs have 10 dynode stages and are operated with a gain  
 45 of  $10^7$  and high voltage around 1200 V (an typical amplified single photoelectron will generate a  
 46  $\approx 6$  mV peak voltage at the input to the front-end amplifiers). The PMTs operate with the anodes  
 47 at high voltage, therefore the signal is AC coupled to the front-end amplifiers. There are two  
 48 versions of AC coupling in the detector both of which use custom designed bifilar-wound 1:1  
 49 toroidal transformers (the DOM specific AC coupling versions, new and old toroids, are shown in  
 50 the right side of Fig. 1). The DOMs with the old toroids were designed with an impedance of  $43\Omega$ ,  
 51 while the new toroids are  $50\Omega$  [8].

52 IceCube relies on two observables per DOM to reconstruct events: the total number of detected  
 53 photons and their timing distribution. Both the timing and the number of photons are extracted from  
 54 the on-board digitized waveforms in software. The waveforms are deconvolved into a series of  
 55 scaled single photoelectron pulses (so-called pulse-series) and the integral of the individual scaled  
 56 pulses (divided by the load resistance) defines the observed charge. It will often be expressed in  
 57 units of PE, or photoelectrons, which further scales the measured charge by the charge of a single  
 58 electron times the nominal gain ( $10^7$ ).

59 When one or more photons produce a charge sufficient to trigger the on-board discriminator  
 60 (set via a DAC to approximately 0.25PE), the signal acquisition process is triggered. The signal  
 61 is feed into four parallel input channels. Three of the channels first pass through a 75 ns delay  
 62 loop in order to capture the leading edge of the pulse, then into three high-speed (300 MSPS for  
 63 128 samples) 10-bit waveform digitizers (Analog Transient Waveform Digitizer, ATWD), each of  
 64 which have a different level of amplification ( $15.7 \pm 0.6$ ,  $1.79 \pm 0.06$ , and  $0.21 \pm 0.01$  [8]). There  
 65 is also three extra ATWDs on-board each DOM: one used for calibration, and the other two operate  
 66 in a ping-pong fashion to remove dead-time associated with the readout. The signal to the fourth  
 67 channel is first shaped and amplified, then feed into a 10-bit fast analog-to-digital converter (fADC)  
 68 operating at a sampling speed of 40 MSPS. Further detail regarding the description of the DOM  
 69 electronics can be found in Refs. [5, 9].

70 This technical report is concerned with accurately determining how the individual DOMs col-  
71 lect charge in order to improve calibration and the description of the detector in the Monte Carlo  
72 simulation. It describes the procedure used to determine the PMTs gain characteristics as seen  
73 in the single photoelectron (SPE) charge distributions using in situ data from the IceCube and  
74 DeepCore detectors. The SPE charge distribution refers to the measured charge probability density  
75 function of the individual DOMs, generated by the amplification of a pure sample of single photo-  
76 electrons. The extraction of the SPE charge distribution was recently made possible by developing  
77 a procedure to reduce the multi-photoelectron (MPE) contamination.

- 78 1. A specially designed unbiased pulse selection was developed to reduce the MPE contami-  
79 nation while accounting for physical phenomena (e.g. late pulses, afterpulses, pre-pulses,  
80 and baseline shifts) and software related effects (e.g. pulse splitting). This will be further  
81 described in Sec. 2.1.
- 82 2. A fitting procedure that separates the remaining MPE contamination from the SPE charge  
83 distribution by deconvolving the measured charged distribution. This is elaborated on in  
84 Sec. 2.3.

85 In using in situ data to determine the SPE charge distributions, we accurately represent the in-  
86 dividual PMT response as a function of time, environmental conditions, software version, hardware  
87 differences, and sample photons uniformly over the surface of the photocathode. This is beneficial  
88 since it also allows us to inspect the stability and long term behavior of the individual DOMs, verify  
89 previous calibration, and correlate features and environment to DOM behavior.

## 90 1.1 Single photoelectron charge distributions

91 In an idealized scenario, a single photon produces a single photoelectron, which is then amplified  
92 by a known amount and the measured charge corresponds to 1PE. However, there are many physical  
93 processes which create structure in the measured charge distributions. For example:

- 94 • **Statistical fluctuation due to cascade multiplication** [10]. At every stage of dynode am-  
95 plification, there is a stochastic spread in the number of emitted electrons that make it to the  
96 next dynode. This in turn causes a spread in the measured charge after the gain stage of the  
97 PMT.
- 98 • **Photoelectron trajectory.** Some electrons may deviate from the favorable trajectory, reduc-  
99 ing the number of secondaries produced at a dynode or the efficiency to collect them on the  
100 following dynode. This can occur at any stage, however, it has the largest effect on the mul-  
101 tiplication at the first dynode [11]. The trajectory of a photoelectron striking the first dynode  
102 will depend on many things, include where on the photocathode it was emitted, the unifor-  
103 mity of the electric field, the size and shape of the dynodes [10], and the ambient magnetic  
104 field [12, 13].
- 105 • **Late or delayed pulses.** A photoelectron can elastically or in-elastically scatter off the first  
106 dynode. The scattered electron can then be re-accelerated to the dynode, creating a second  
107 pulse. The difference in time between the initial pulse and the re-accelerated pulse in the

108 R7081-02 PMT was previously measured to be up to 70 ns [7, 14]. The two sub-pulses have  
109 lower chargers, but the sum of the two tends to add up to the original charge. Collecting either  
110 the initial pulse or the late pulse will result in the charge being reconstructed as lower [15].

111 • **Afterpulses.** When a photoelectron or the secondary electrons produced during the electron  
112 cascade gain sufficient energy to ionize residual gas in the PMT, the positively charged ion-  
113 ized gas will be accelerated in the electric field towards the cathode. Upon impact with the  
114 photocathode, electrons can be again released from the photocathode, creating what is called  
115 an afterpulse. For the R7081-02 PMTs, the timescale for afterpulses was measured to occur  
116 from 0.3 to 11  $\mu$ s after the initial pulse, with the first prominent afterpulse peak occurring at  
117 approximately 600 ns [7]. The spread in the afterpulse time is dependent on the position of  
118 photocathode, the charge to mass ratio of the ion produced, and the electric potential distri-  
119 bution [16]; whereas the size of the afterpulse is related to the momentum and species of the  
120 ionized gas and composition of the photocathode [17].

121 • **Pre-pulses.** If an incident photon passes through the photocathode without interaction and  
122 strikes one of the dynodes, it can eject an electron that is only amplified by the subsequent  
123 stages, resulting in a lower measured charge (lower by a factor of approximately 25). For the  
124 IceCube PMTs, the pre-pulses were found to arrive approximately 30 ns before the signal  
125 from other photoelectrons from the photocathode [7].

126 • **Multi-PE contamination.** When multiple photoelectrons arrive at the first dynodes within  
127 several nanoseconds of each other, they can be reconstructed by the software as a single,  
128 multi-PE pulse.

129 • **Electronic noise.** This refers to the fluctuations in the analog-to-digital converters (ATWDs  
130 and FADC) and ringing arising from the electronics.

131 Beyond the physical phenomena above that modify the measured charge distribution, there is  
132 also a lower limit to the smallest charge that can be extracted. For IceCube, the discriminator limits  
133 the trigger pulse to be above 0.25PE, and subsequent pulses in the readout time window are subject  
134 to a software defined threshold. The software threshold was set conservatively to avoid extracting  
135 pulses that originated from electronic noise. This threshold can be modified to gain access to lower  
136 charge pulses, and will be discussed in Sec. 2.2.

137 The standard charge distribution model used by the IceCube collaboration (known as the  
138 TA0003 distribution) represented the above effects as the sum of an exponential plus a Gaussian,  
139 where the exponential represented charge of poorly amplified pulses, and the Gaussian represented  
140 the spread in statistical fluctuations due to the cascade multiplication. A description of the TA0003  
141 model can be found in Ref. [7]), and the average distribution was previously used to describe all  
142 the PMTs in the IceCube and DeepCore detectors.

143 Recently, IceCube has performed several lab measurements using the R7081-02 PMTs with in-  
144 time laser pulses, demonstrating that the in-time charge distribution includes a steeply falling low-  
145 charge component below the discriminator threshold. To account for this, a new functional form  
146 including a second exponential was introduced. This form of the charge distribution,  $f(q)_{SPE} =$   
147  $Exp_1 + Exp_2 + \text{Gaussian}$ , is referred to as the *SPE template* in this report. Explicitly:

$$f(q)_{SPE} = E_1 e^{-q/w_1} + E_2 e^{-q/w_2} + N e^{-\frac{(q-\mu)^2}{2\sigma^2}}. \quad (1.1)$$

148 Where  $q$  represents the measured charge;  $E_1$ ,  $E_2$ , and  $N$  represent normalization factors of  
 149 each components;  $w_1$  and  $w_2$  are the exponential decay widths; and  $\mu$ ,  $\sigma$  are the Gaussian mean  
 150 and width respectively. This is the assumed functional shape of the SPE charge distributions and  
 151 the components of Eq. 1.1 are determined in this report for all in-ice DOMs. IceCube defines 1PE  
 152 as the location of the Gaussian mean ( $\mu$ ) and calibrates the gain on the individual PMTs during the  
 153 start of each season to meet this definition.

## 154 1.2 IceCube datasets and software definitions

155 The largest contribution to the IceCube trigger rate comes from down-going muons produced in  
 156 cosmic ray induced showers [18]. Cosmic ray muons stopping in the detector cause the individual  
 157 trigger rate to decrease at lower depths. Further, during the formation of this ice sheet, there have  
 158 been several periods of colder climate that have caused different optical properties in the ice at  
 159 different depths. The optical properties also affect the trigger rate, in particular, the “dust layer”  
 160 from 2100 to 2200 m (optical modules 32-38 in the IceCube detector) below the surface is a region  
 161 in the ice with a relatively large scattering and absorption coefficient [19].

162 An induced signal in the PMT will pass through the AC coupling toroid located on the base  
 163 of the PMT, then be compared to a discriminator threshold set to 0.25PE. If two adjacent DOMs  
 164 observe a passing of the discriminator, a *Hard Local Coincidence* (HLC) is initiated and the corre-  
 165 sponding waveforms are sampled 128 times and readout on the three ATWDs.

166 After waveform digitization, there is a correction applied to remove any DC baseline offset  
 167 and correct for the signal droop and undershoot introduced by either version of the AC coupling.  
 168 Scaled SPE pulse templates (that take into account the version of the AC coupling) are then fit to  
 169 the waveforms using software referred to as WaveDeform, which determines the individual pulse  
 170 time stamp and charge, and populates a pulse series.

171 The pulse series used in this analysis come from two datasets provided by IceCube:

172 1. The **MinBias dataset**. This dataset records the full waveform readout of randomly triggered  
 173 HLC events, at a rate that corresponds on average to 1/1000 events. The largest contribution  
 174 to the IceCube trigger rate comes from down-going muons produced in cosmic ray induced  
 175 showers [18] and therefore is the largest signal component in this dataset. The full waveform  
 176 of these events allows us to extract the raw information about the individual pulses and  
 177 therefore, this will be used to measure the individual PMT charge distributions.

178 2. The **BeaconLaunch dataset**. This is a forced-trigger (not triggered by the discriminator)  
 179 filter that is typically used to monitor the individual DOM baseline. It therefore also in-  
 180 cludes the full ATWD window waveform readout. Since this dataset is forced-triggered, the  
 181 majority of these waveforms represent baseline fluctuations, however there will be the occa-  
 182 sional coincidental pulse that makes it into the readout window. This dataset will be used to  
 183 examine the noise contribution to the charge distributions. Note: when using this datasets,  
 184 the weight of every pulse is scaled by a factor of 28.4 to account for the livetime difference  
 185 between the MinBias dataset and the BeaconLaunch dataset.



186 This analysis uses the full MinBias and BeaconLaunch datasets from IceCube season 2011  
 187 to 2016 (subsequently referred to as IC86.2011 to IC86.2016). Seasons in IceCube typically start  
 188 in June of the labeled year and end approximately one year later. Calibration is performed at the  
 189 beginning of each season.

## 190 2. Extracting the SPE templates

### 191 2.1 Single photoelectron pulse selection

192 The pulse selection is the method used to extract candidate, unbiased, single photoelectron pulses  
 193 from data, while minimizing the multi-PE contamination. It avoids collecting afterpulses, rejects  
 194 late pulses from the trigger, reassembles late pulses, accounts for the discriminator threshold,  
 195 reduces the effect of droop and baseline undershoot, and gives sufficient statistics to perform a  
 196 season-to-season measurement. An illustrative diagram of the pulse selection is shown in the left  
 197 side of Fig. 2, while a description of the procedure is detailed below.

198 In order to trigger a DOM, the input to the front-end amplifiers must exceed the discriminator  
 199 threshold. To avoid the selection bias of the discriminator trigger, we ignore the trigger pulse as  
 200 well as the entire first 100 ns of the time window. Ignoring the first 100 ns has the added benefit  
 201 of also removing late pulses that could be attributed to the triggering pulse. To ensure we are not  
 202 accepting afterpulses into the selection, we also enforce that the pulse of interest (POI) is within the  
 203 first 375 ns of the ATWD time window. In the vicinity of the POI, we check that WaveDeform did  
 204 not reconstruct any pulses up to 50 ns prior to the POI, or 100-150 ns after the POI (the light-gray  
 205 region of Fig. 2 Left). This later constraint is to reduce the probability of accidentally splitting a  
 206 late pulse in the summation window.

207 Restrictions are put on the full ATWD waveforms as well, such as ensuring that the trigger  
 208 pulse does not exceed 10 mV (to reduce the effect of the subsequent baseline undershoot due to

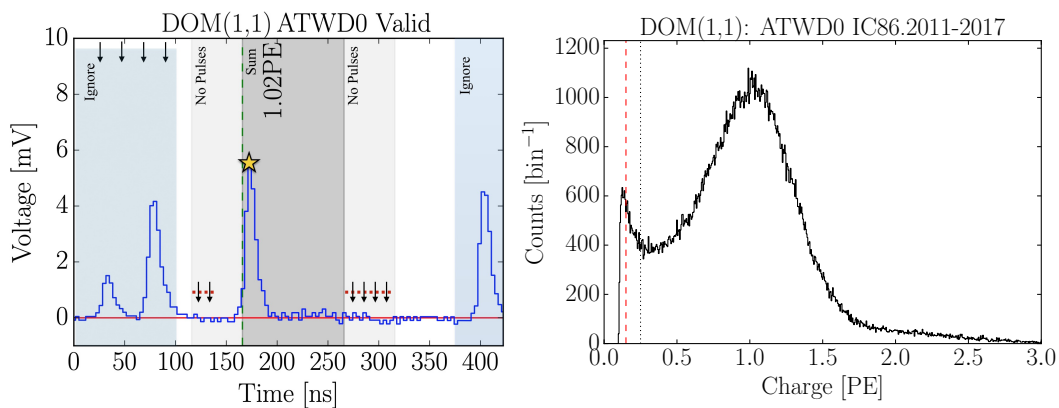


**Figure 2.** Left: An illustrative diagram of the pulse selection criteria for selecting a high purity and unbiased sample of single photoelectrons. The pulse of interest is identified with the yellow star. We see a small trigger pulse at 25 ns (due to the delay board), followed by a potential late pulse. At 400 ns, we see a pulse in the region susceptible to afterpulses. Right: The collected charges from string 1, optical module 1 (DOM 1,1), from the MinBias data collected from IC86.2011 to IC86.2016 using the pulse selection. The discriminator threshold at 0.25PE is shown as a dotted black vertical line. For visual purposes, a dotted-red line is also included at 0.15PE.

209 the AC coupling or other artifacts from large pulses) as well as a global constraint that the time  
 210 window cannot contain any pulses that exceeds 20 mV.

211 If a pulse is reconstructed between 100 and 375 ns after the time window is opened and the  
 212 voltage criteria is met, it is accepted as a candidate photoelectron and several checks are performed  
 213 on the waveform prior-to and after the pulse. The first check is to ensure that the waveform is  
 214 near the baseline just prior to the rising edge of the POI. This is accomplished by ensuring that  
 215 the waveform does not exceed 1 mV, 50 to 20 ns prior to the POI, and eliminates cases where the  
 216 POI is a late pulse. We also ensure the waveform returns to the baseline by checking that no ADC  
 217 measurement exceeds 1 mV, 100 to 150 ns after the POI (these constraints are illustrated as the  
 218 red-dotted lines and black arrows in Fig. 2 Left).

219 If all the above criteria are met, we sum the reconstructed charges from the POI time (given  
 220 by WaveDeform) to +100 ns (the dark gray area of in Fig. 2 Left). This ensures that any nearby  
 221 pulses are either fully separated or fully added (in-case WaveDeform incorrectly split the pulse,  
 222 and to reassemble late pulses). The 100 ns summation also means that the pulse selection we will  
 223 occasionally be accepting MPE events.

## 224 2.2 Characterizing the low-charge region

225 Fig. 2 (right) shows the charge distribution in black of the selected pulses that pass the single  
 226 photoelectron pulse selection for string 1, optical module 1 (DOM (1,1)). In the low-charge re-  
 227 gion (below 0.25PE), we see a steep rise (in agreement with the in-time laser tests mentioned in  
 228 Sec. 1.1), then a second threshold at approximately 0.13PE. This is a software defined threshold  
 229 that comes from WaveDeform not attempting to deconvolve charges smaller than a predefined size.  
 230 The threshold was set to avoid electronic noise being interpreted as PMT pulses and contaminating  
 231 the low-charge region. This section will examine the effect on the charge distribution and noise  
 232 contribution by lowering the WaveDeform threshold. The aim will be to explore the low-charge  
 233 region.

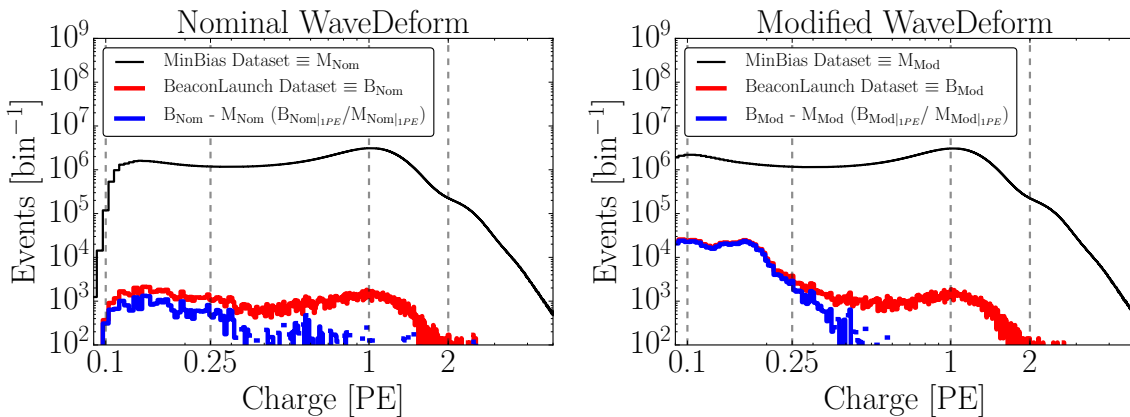


**Figure 3.** The cumulative charge distributions (IC86.2011-2016) of all DOMs for the MinBias and BeaconLaunch datasets. The blue histogram shows the expected contribution from noise (found by subtracting the shape of the MinBias dataset from the BeaconLaunch dataset). Left: The charge distributions for the standard WaveDeform settings. Right: The charge distributions for the modified WaveDeform settings.



234 Fig. 3 (left) shows the charge distributions for the MinBias (black) and the BeaconLaunch  
 235 (red) datasets using the default settings on WaveDeform. As mentioned in Sec. 1.2, occasionally  
 236 a photoelectron will be coincident with the forced BeaconLaunch time window and populate a  
 237 single photoelectron distribution. Subtracting the shape of the MinBias charge distribution from the  
 238 BeaconLaunch dataset yields an estimate of the amount of electronic noise contamination (blue).  
 239 The bin with the largest signal-to-noise ratio (SNR) above 0.1PE was found to have 0.0013. The  
 240 SNR for the the full distribution was found to be 0.0005. Fig. 3 (right) shows the same data after  
 241 lowering the WaveDeform threshold. Correspondingly, the bin with the largest SNR was found to  
 242 be 0.0017, whereas the total SNR was found to be 0.0015.

### 243 2.3 Fitting procedure

244 The fit assumes that there is a negligible three-PE contribution, which is justified by the lack of  
 245 statistics in the 3PE region as well as the significant scale difference between the 1PE and 2PE  
 246 region, as shown in Fig. 2 (right). The 2PE charge distribution is assumed to be the SPE charge  
 247 distribution convolved with itself [20]. A python-based piece of software called the "convolutional  
 248 fitter" is used to determine the components of Eq. 1.1 from the measured charge distribution that  
 249 includes the multi-PE contamination.

250 The  $\text{Exp}_2$  component (as well as the  $\text{Exp}_1$ ) of Eq. 1.1, represents poorly amplified photoelec-  
 251 trons and therefore we do not allow it to extend beyond the high charge region of the Gaussian  
 252 component. In particular, we include a constraint on the parameter  $w_2$  to ensure that it falls off  
 253 with the Gaussian component:

$$w_2 < \frac{\mu + 2\sigma}{4 - \text{Ln}(N/E_2)}. \quad (2.1)$$

254 This equation was found by setting the  $\text{Exp}_2$  to be  $1/e^2$  that of the Gaussian component at two  
 255 sigma (the  $\text{Exp}_1$  is neglected from this equation since it falls off in the low-charge region). Eq. 2.1  
 256 is used as a constraint during the fit to the charge distributions.

257 Pulses that fall below the WaveDeform threshold and are not reconstructed contribute to an  
 258 effective efficiency of the individual DOMs. This analysis assumes the same shape of the steeply  
 259 falling exponential component ( $\text{Exp}_1$ ) for all DOMs in the detector to avoid large fluctuations in  
 260 the individual DOM efficiencies. The modified WaveDeform data will strictly be used to deter-  
 261 mining the average low-charge region. Specifically, we will fit the cumulative charge distribution  
 262 to determine the components of Eq. 2.1 with the modified WaveDeform, background subtract the  
 263 BeaconLaunch data, and only use the measured shape and normalization of  $\text{Exp}_1$  in all subsequent  
 264 non-modified WaveDeform fits.

265 The  $\text{Exp}_1$  component is inserted into the non-modified WaveDeform fits and the SPE templates  
 266 are extracted. The residual of the fit compared to data is calculated and expressed as a percentage  
 267 difference. The average residual of all DOMs is then calculated and used as global scaling factor  
 268 for all SPE templates.

269 Failed fits (DOMs removed from service (109 DOMs) and DOMs that fail any one of several  
 270 validity checks on the goodness of fit (6 DOMs)) are not included in this report, however, in the  
 271 MC software chain they are assigned the AVG charge distribution.

272 **2.4 SPE template fit results**

273 Using the background subtracted modified WaveDe-  
 274 form dataset, the steeply falling exponential compo-  
 275 nent was determined by fitting from 0.1PE to 3.5PE  
 276 to be  $E_1 = 6.9 \pm 1.5$  and  $w_1 = 0.032 \pm 0.002$ PE. The  
 277 shape of the steeply falling exponential is then used to  
 278 describe the low-PE charge region for all subsequent  
 279 non-modified WaveDeform fits.

280 Using the non-modified WaveDeform dataset with  
 281 the value for  $E_1$  described above, the SPE templates are  
 282 extracted for every DOM, separately for each IceCube  
 283 season (IC86.2011 to IC86.2016). An average fit was  
 284 also performed in which all the data was summed to-  
 285 gether (labeled as "AVG"). The fit range for  $\text{Exp}_2$  and the Gaussian components are selected to be  
 286 between 0.15PE and 3.5PE. The average residual for all DOMs from 0 to 1PE is shown in Fig. 4.

287 An example fit is shown in Fig. 5 for the cumulative charge distribution for DOM (1,1). The  
 288 collected charge distribution is shown in the black histogram, while the convolutional fit is shown  
 289 as the black line (scaled by the residual). The extracted SPE template (also scaled by the residual)  
 290 for this DOM is shown in red. The 2PE contribution from the fit is shown in blue.

291 The mean value and  $1\sigma$  spread of the fit parameters, excluding  $\text{Exp}_1$ , for the IceCube and

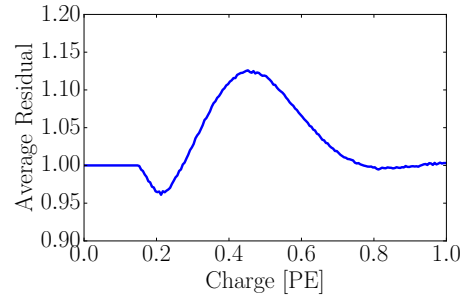


**Figure 4.** The measured average residual of the SPE templates fit.

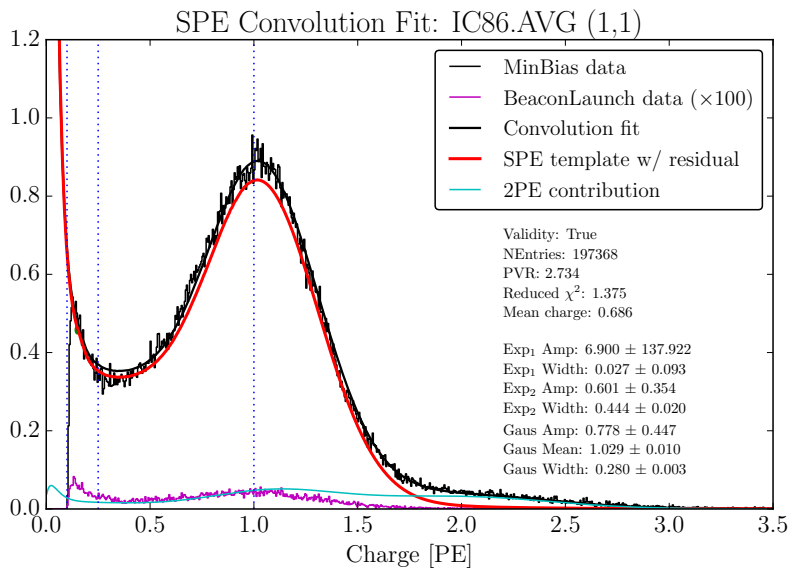


**Figure 5.** An example fit result for DOM (1,1) using the non-modified WaveDeform dataset from all seasons. The result from the convolutional fitter is shown in black. The extracted SPE template is shown in red. The purple histogram is the full detector (all DOMs summed together) non-modified BeaconLaunch dataset, scaled to the livetime of the MinBias data and further multiplied by a factor of 100 in order to be visible on this plot.

292 DeepCore detectors are shown in Table 1 and Table 2 respectively.

293 The individual DOM SPE templates were then examined between IceCube seasons for a time  
 294 dependence on the fit parameters. For every DOM, the change over time of each fit parameter  
 295 (excluding  $\text{Exp}_1$ ) was calculated.

IceCube	$\text{Exp}_2$ Amplitude	$\text{Exp}_2$ Width	Gaus. Amplitude	Gaus. Mean	Gaus. Width
IC86.2011	$0.601 \pm 0.101$	$0.457 \pm 0.070$	$0.736 \pm 0.061$	$1.022 \pm 0.030$	$0.296 \pm 0.033$
IC86.2012	$0.595 \pm 0.100$	$0.462 \pm 0.065$	$0.740 \pm 0.062$	$1.020 \pm 0.034$	$0.295 \pm 0.033$
IC86.2013	$0.602 \pm 0.101$	$0.452 \pm 0.071$	$0.736 \pm 0.060$	$1.021 \pm 0.033$	$0.298 \pm 0.032$
IC86.2014	$0.597 \pm 0.099$	$0.453 \pm 0.071$	$0.736 \pm 0.059$	$1.019 \pm 0.030$	$0.299 \pm 0.030$
IC86.2015	$0.604 \pm 0.099$	$0.457 \pm 0.067$	$0.735 \pm 0.061$	$1.024 \pm 0.032$	$0.296 \pm 0.032$
IC86.2016	$0.600 \pm 0.101$	$0.460 \pm 0.063$	$0.736 \pm 0.060$	$1.024 \pm 0.030$	$0.295 \pm 0.031$

**Table 1.** The average fit value and  $1\sigma$  spread for the IceCube detector. The active DOMs in the IceCube detector are 99.4% normal quantum efficiency and 31.0% of the DOM have the original method of AC coupling. Correspondingly, there are 0.6% HQE DOMs and 69.0% of the DOM have the new version of AC coupling.

DeepCore	$\text{Exp}_2$ Amplitude	$\text{Exp}_2$ Width	Gaus. Amplitude	Gaus. Mean	Gaus. Width
IC86.2011	$0.519 \pm 0.095$	$0.462 \pm 0.099$	$0.763 \pm 0.073$	$1.023 \pm 0.031$	$0.307 \pm 0.038$
IC86.2012	$0.517 \pm 0.095$	$0.467 \pm 0.098$	$0.763 \pm 0.074$	$1.024 \pm 0.032$	$0.306 \pm 0.038$
IC86.2013	$0.520 \pm 0.092$	$0.461 \pm 0.096$	$0.763 \pm 0.073$	$1.024 \pm 0.030$	$0.306 \pm 0.037$
IC86.2014	$0.522 \pm 0.093$	$0.459 \pm 0.098$	$0.765 \pm 0.073$	$1.021 \pm 0.031$	$0.306 \pm 0.038$
IC86.2015	$0.525 \pm 0.095$	$0.458 \pm 0.099$	$0.763 \pm 0.072$	$1.023 \pm 0.031$	$0.307 \pm 0.038$
IC86.2016	$0.522 \pm 0.095$	$0.464 \pm 0.098$	$0.763 \pm 0.074$	$1.024 \pm 0.031$	$0.305 \pm 0.038$

**Table 2.** The average fit value and  $1\sigma$  spread for the DeepCore detector. The active DOMs in DeepCore are 12.4% NQE DOMs and 0.2% of the DOM have the original method of AC coupling. Correspondingly, the DeepCore contains 87.6% HQE DOMs and 99.8% of the DOM have the new version of AC coupling.

296 Fig. 6 shows the change in a given fit parameter (represented in percentage deviation from the  
 297 mean value), per year, of each DOM in both the IceCube (left) and DeepCore (right) detectors.  
 298 The spread in the fit parameters were found to be consistent with statistically scrambling the yearly  
 299 measurements. All the fit parameters are found to deviate less than 0.1% per year in both detectors,  
 300 which is in agreement with the stability checks performed in Ref. [8].

### 301 3. Discussion

#### 302 3.1 Correlations between fit parameters and DOM hardware differences

303 As noted in Sec. 1, there are two DOM-related hardware differences: the subset of HQE DOMs  
 304 and the version of AC coupling used to couple the signal from the PMT anode to the front-end am-  
 305 plifiers. Correlations between the different hardware configurations were examined for correlations  
 306 with the SPE template fit components.

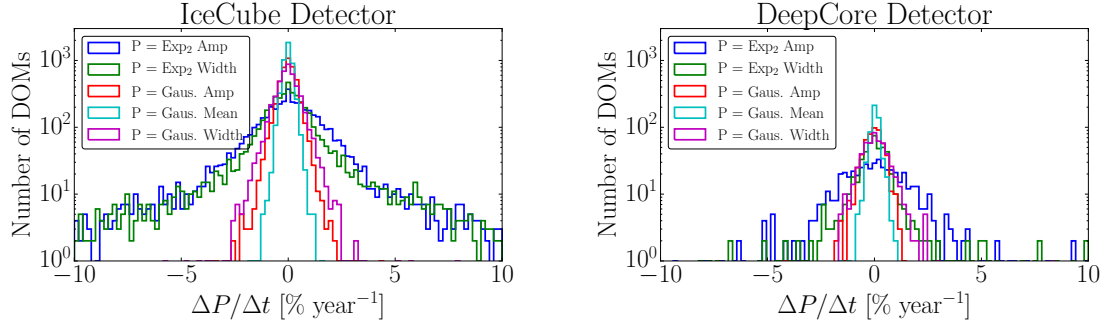


**Figure 6.** The change in individual DOM fitted parameters over time (Left: IceCube, Right: DeepCore). The change in the fit value is represented in percentage deviation from the mean fit parameter value.

307 The HQE DOMs were found to have a larger  $\text{Exp}_2$  component (2.3% lower  $w_2$  component,  
 308 and a 19.9% higher  $E_2$ , described in terms of Eq.1.1) than the standard DOMs<sup>1</sup>. Consequently,  
 309 the HQE DOMs have an 14.9% lower peak-to-valley ratio and a 3.3% lower mean charge. These  
 310 distributions are shown in Fig. 7.

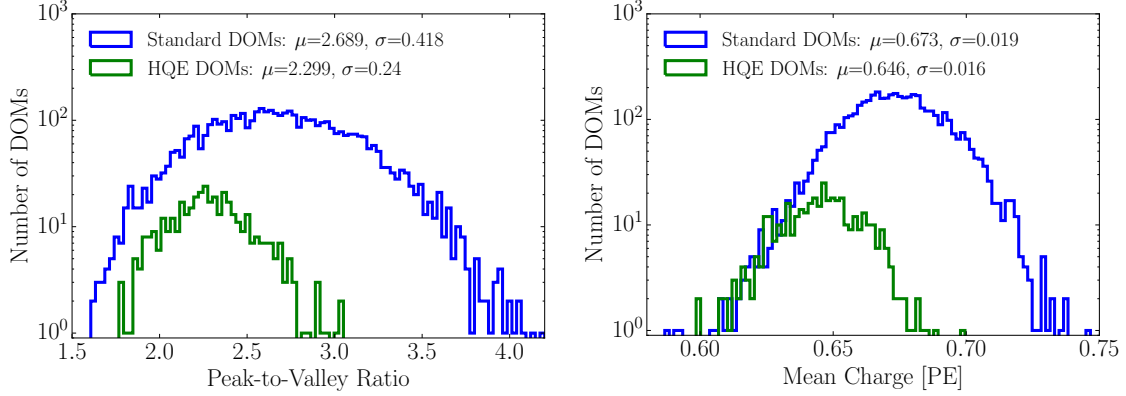


**Figure 7.** Comparison between the R7081-02MOD HQE DOMs and standard R7081-02 DOMs. Left: The Peak-to-Valley ratio for the two subsets of quantum efficiencies. Right: The mean charge of the individual DOM SPE templates.

311 The subset of NQE DOMs with the original AC coupling transformer were found to have a  
 312 6.1% narrower Gaussian width and an 8.0% larger Gaussian amplitude ( $\sigma$  and  $N$  in Eq. 1.1). The  
 313 exponential component  $\text{Exp}_2$  was also found to have a 7.5% lower  $E_2$  component, and a 3.0%  
 314 higher  $E_2$  component. Although the old toroid DOMs were deployed into ice earlier than the new  
 315 toroid DOMs, the difference above is still noted when examining individual deployment years,  
 316 therefore the shape differences are not attributed to the change in the DOM behavior over time.  
 317 However, the DOMs with the old toroids used the first PMTs to be manufactured by Hamamatsu,  
 318 therefore, this difference may also be attributed to a gradual change in the process parameters over  
 319 the course of the PMT manufacturing change in the production procedure rather than the actual AC  
 320 coupling version. (Spencer: I've checked this, if the PMTSerial is sequential with the production  
 321 date, this is not attributed to manufacturing).

<sup>1</sup>This difference is still observed when comparing the DOMs at similar depths in the detector.

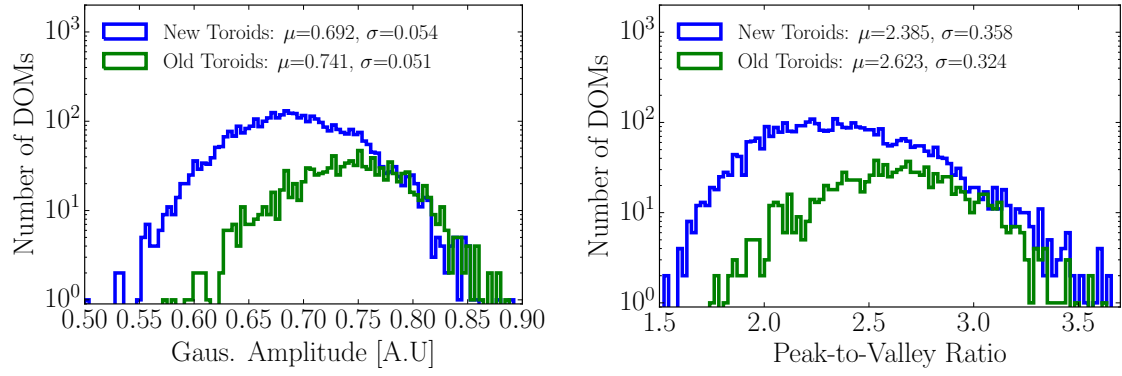


**Figure 8.** Comparison between the AC coupling version used on the NQE DOMs. Left: The distribution of the measured Gaussian amplitudes. Right: The distribution of the measured Peak-to-Valley ratios.

### 3.2 Quantifying observable changes when modifying the PMT charge distributions

Changing the assumed gain response in simulation, as deduced from data, has different implications depending on the typical illumination level as present in different analysis. These differences are outlined in the following.

The PMT response is described by a combination of a "bare" efficiency,  $\eta_0$ , and a normalized charge response function,  $f(q)$ . The bare efficiency represents the fraction of arriving photons that result in any non-zero charge response, including those well below the discriminator threshold. The normalization condition is:

$$\int_0^{\text{inf}} f(q) dq = 1. \quad (3.1)$$

Generally,  $f(q)$  and  $\eta_0$  have to be adjusted together to maintain agreement with a quantity known from lab or in-ice measurements, such as the predicted number of pulses above threshold for a dim source.

**Dim source measurements** Where light levels are low enough, sub-discriminator pulses do not contribute any observed charge because they do not satisfy the trigger threshold and the probability of two photons arriving together is negligible. Given some independent way of knowing the number of arriving photons, a lab or in-ice measurement determines the trigger fraction above threshold  $\eta_{0.25}$  and/or the average charge over threshold  $Q_{0.25}$ , either of which can be used to constrain the model as follows:

$$\eta_{0.25} = \eta_0 \int_{0.25q_{pk}}^{\text{inf}} f(q) dq \quad (3.2)$$

$$Q_{0.25} = \eta_0 \int_{0.25q_{pk}}^{\text{inf}} qf(q) dq \quad (3.3)$$

Here, the discriminator threshold is assumed to be 0.25 times the peak position  $q_{pk}$ . It is also useful to scale observed charges by  $q_{pk}$ , since we set each PMT gain by such a reference, and then a measurement constraint would be stated in terms of  $Q_{0.25}/q_{pk}$ .

342 **Semi-bright source measurements** Once the ATWD window is open, subsequent pulses are not  
 343 limited by the discriminator threshold, however, WaveDeform introduces a software threshold at  
 344 0.1PE (described at the end of Section 2.1). The average charge of an individual pulse that arrive  
 345 within the time window is therefore:

$$Q_{0.10} = \eta_0 \int_{0.10q_{pk}}^{\text{inf}} qf(q)dq \quad (3.4)$$

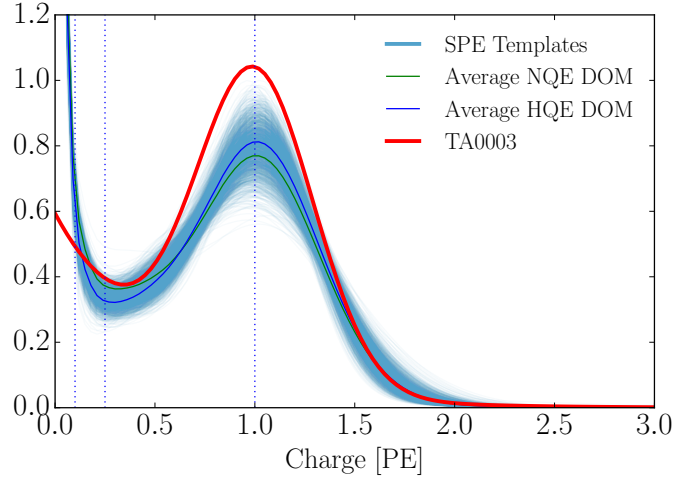


**Figure 9.** Left: The normalized charge distributions. The TA0003 distribution is shown in red, while the cumulative SPE templates for DOMs in both IceCube and DeepCore are shown in Blue. Right: An analysis level comparison for the TA0003 distribution compared to the SPE Templates to the full data from IC86.2017.

346 **Bright source measurements** For light levels that are large, the trigger is satisfied regardless  
 347 of the response to individual photons, and the total charge per arriving photon therefore includes  
 348 contributions below both the discriminator and the WaveDeform thresholds:

$$Q_0 = \eta_0 \int_0^{\text{inf}} qf(q)dq \quad (3.5)$$

349 As such the total charge is directly proportional to the average charge of the SPE template,  
 350 having a strong dependence on the steeply falling exponential.

### 351 3.2.1 Model comparison

352 When the charge distribution model is changed in a way that preserves agreement with the mea-  
 353 sured  $\eta_{0.25}$  or  $Q_{0.25}/q_{pk}$ , i.e.  $\eta_0$  is adjusted properly for changes in  $f(q)$ , the physical effect can be  
 354 summarized by the change in the bright-to-dim ratios  $Q_0/Q_{0.25}$ , and  $Q_0/Q_{0.10}$ . Conveniently, these  
 355 ratios depend only on the shape of  $f(q)$ . Table 3 compares these ratios in terms of the previous  
 356 charge distribution (TA0003) and the SPE templates described here.



Model	Detector	$Q_0/Q_{0.25}$	$Q_0/Q_{0.10}$	$\eta_{0.25}/Q_{0.25}$
TA0003	IceCube and DeepCore	1.017	1.003	0.969
SPE Templates	IceCube	$1.031\pm 0.003$	$1.013\pm 0.001$	$0.971\pm 0.006$
SPE Templates	DeepCore	$1.034\pm 0.002$	$1.014\pm 0.001$	$0.965\pm 0.006$

**Table 3.** The distribution in bright-to-dim ratios for the previous charge distribution (TA0003) and the individual DOM SPE templates for the IceCube and DeepCore detector.

357 Table 3, shows percent-level differences in the physically observable bright-to-dim ratios.  
358 Fig. 9 shows the shape difference between the TA0003 distribution and all the SPE templates  
359 measured in this report. The shape difference is attributed to a better control of the low-charge  
360 region, the difference in functional form (described in Section 1.1), as well as the fact that the SPE  
361 templates sample uniformly over the entire photocathode at random incident angles.

### 362 3.3 SPE templates in simulation

363 The IceCube Monte Carlo simulation chain assigns a charge to every photoelectron generated at  
364 the surface of the photocathode. The charge is determined by sampling from a normalized charge  
365 distribution. A comparison between describing the charge distribution using the SPE templates  
366 compared to the TA0003 distribution follows.

367 Two simulation sets consisting of the same set of events were processed through the IceCube  
368 Monte Carlo simulation chain to the final level of the multi-year High Energy Sterile Analysis. At  
369 analysis level, the events that pass the cuts are  $>99.9\%$  pure up-going (directed upwards relative  
370 to the horizon) secondary muons produced by charged current muon neutrino interactions. The  
371 energy range of this event selection is between 500GeV-10TeV in reconstructed quantities.

372 Fig. 10 (left) shows the distribution of the total measured charge in a single DOM during each  
373 event. The data is shown for the full IC86.2012 season, but statistically equivalent to any of the  
374 other seasons. The simulation set using the TA0003 charge distribution is shown in orange, and the  
375 SPE Templates is shown in blue. The bottom of the plot shows the ratio of the measured quantity  
376 relative to data.

377 Fig. 10 (right) shows the distribution of the measured total charge on a DOM (after noise  
378 removal) divided by the number of channels, or DOMs, that participated in the event.

### 379 3.4 SPE templates for calibration

380 IceCube calibrates the gain setting at the beginning of the season such that the Gaussian mean  
381 charge distribution corresponds to a gain of  $10^7$  (equivalently labelled as 1PE). Since the method  
382 used to extract the Gaussian mean described in this report is different from the previous method  
383 used for calibration of the DOMs the total measured charge from a DOM is expected to change  
384 with the updated calibration.

385 As shown in Table 1, the Gaussian mean component of the fit of every year is found to be  
386 on average 2.2% higher than unity, corresponding to a systematic overestimation of the measured  
387 charge in the detector along with a standard deviation of 3.1%. This correction to the measured  
388 charge can be implemented by dividing the reported charge from WaveDeform by the correspond-

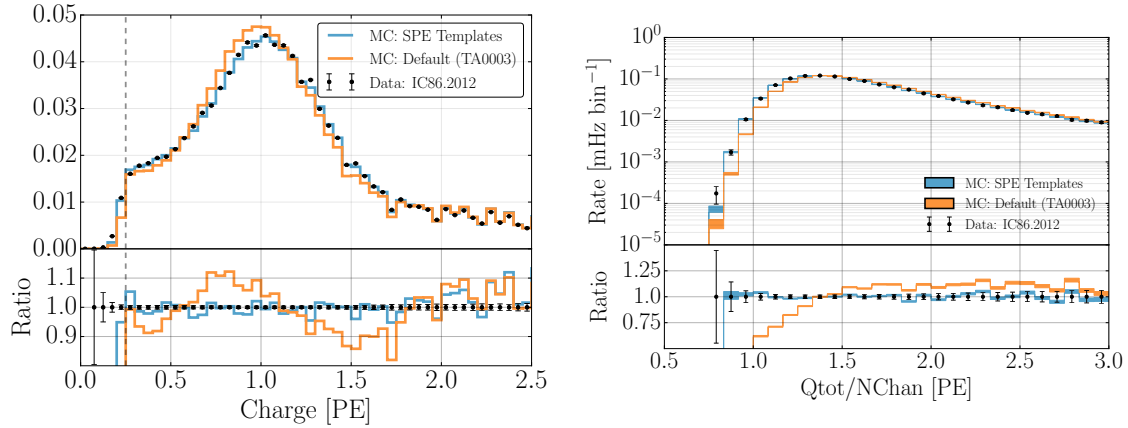


**Figure 10.** A comparison between the SPE Templates (blue) and the TA0003 (orange) model for describing the SPE charge distribution in Monte Carlo. The simulation is compared to the 2012 IceCube season. Left: The total measured charge per DOM, per event at analysis level. Right: The distribution of the total measured charge of an event divided by the number of DOMs that participated in the event.

389 ing Gaussian mean for a given DOM. This can be done retroactively in IceCube by reprocessing  
 390 the data (commonly referred to as a "Pass").

#### 391 4. Conclusion

392 This report outlines the procedure used for collecting a relatively pure sample of single photoelec-  
 393 tron charges for each of the in-ice DOMs in IceCube. Multi-PE contamination was removed using  
 394 the assumption that the MPE contamination is the convolution of the SPE distribution multiple  
 395 times.

396 The SPE templates were extracted for each DOM and each season in the IceCube and Deep-  
 397 Core detectors, and investigated for correlations with hardware related features. Both detectors do  
 398 not show more than a 0.5% deviation in any of the fitted parameters over the investigated seasons,  
 399 in agreement with Ref. [8]. Yearly variations in the fit parameters are consistent with statistical  
 400 fluctuations. The HQE DOMs located in the IceCube and DeepCore detectors were found to have  
 401 a distinguishable Exp<sub>2</sub> component from the standard DOMs. Similarly, DOMs with the original  
 402 method of AC coupling were found to have a narrower and larger Gaussian component. This was  
 403 not found to be due to a manufacturing process, however is still under investigation.

404 The SPE templates were implemented into the MC simulation chain and show an improvement  
 405 in the overall description of charge in the detector. Modern IceCube simulation sets use this update.

406 The new method for extracting the calibration constant that determines the gain setting on each  
 407 of the PMTs (the Gaussian mean of the fit), has been revised and shows that the average gain was  
 408 approximately  $2.2\% \pm 3.1\%$  higher than expected.

#### 410 Acknowledgments

411 We acknowledge the support from the following agencies: U.S. National Science Foundation - Of-

412 fice of Polar Programs, U.S. National Science Foundation - Physics Division, University of Wiscon-  
413 sin Alumni Research Foundation, the Grid Laboratory Of Wisconsin (GLOW) grid infrastructure  
414 at the University of Wisconsin - Madison, the Open Science Grid (OSG) grid infrastructure; U.S.  
415 Department of Energy, and National Energy Research Scientific Computing Center, the Louisiana  
416 Optical Network Initiative (LONI) grid computing resources; Natural Sciences and Engineering  
417 Research Council of Canada, WestGrid and Compute/Calcul Canada; Swedish Research Coun-  
418 cil, Swedish Polar Research Secretariat, Swedish National Infrastructure for Computing (SNIC),  
419 and Knut and Alice Wallenberg Foundation, Sweden; German Ministry for Education and Re-  
420 search (BMBF), Deutsche Forschungsgemeinschaft (DFG), Helmholtz Alliance for Astroparticle  
421 Physics (HAP), Research Department of Plasmas with Complex Interactions (Bochum), Germany;  
422 Fund for Scientific Research (FNRS-FWO), FWO Odysseus programme, Flanders Institute to en-  
423 courage scientific and technological research in industry (IWT), Belgian Federal Science Policy  
424 Office (Belspo); University of Oxford, United Kingdom; Marsden Fund, New Zealand; Australian  
425 Research Council; Japan Society for Promotion of Science (JSPS); the Swiss National Science  
426 Foundation (SNSF), Switzerland; National Research Foundation of Korea (NRF); Villum Fonden,  
427 Danish National Research Foundation (DNRF), Denmark.

428 **References**

- 429 [1] J. Ahrens *et al.*, “Icecube preliminary design document,” URL: <http://www.icecube.wisc.edu/science/publications/pdd>, 2001.  
430
- 431 [2] A. Achterberg, M. Ackermann, J. Adams, J. Ahrens, K. Andeen, D. Atlee, J. Baccus, J. Bahcall,  
432 X. Bai, B. Baret, *et al.*, “First year performance of the icecube neutrino telescope,” *Astroparticle*  
433 *Physics*, vol. 26, no. 3, pp. 155–173, 2006.
- 434 [3] I. Collaboration *et al.*, “Evidence for high-energy extraterrestrial neutrinos at the icecube detector,”  
435 *Science*, vol. 342, no. 6161, p. 1242856, 2013.
- 436 [4] R. Abbasi, Y. Abdou, T. Abu-Zayyad, M. Ackermann, J. Adams, J. Aguilar, M. Ahlers, M. Allen,  
437 D. Altmann, K. Andeen, *et al.*, “The design and performance of icecube deepcore,” *Astroparticle*  
438 *physics*, vol. 35, no. 10, pp. 615–624, 2012.
- 439 [5] R. Abbasi, M. Ackermann, J. Adams, M. Ahlers, J. Ahrens, K. Andeen, J. Auffenberg, X. Bai,  
440 M. Baker, S. Barwick, *et al.*, “The icecube data acquisition system: Signal capture, digitization, and  
441 timestamping,” *Nuclear Instruments and Methods in Physics Research Section A: Accelerators,*  
442 *Spectrometers, Detectors and Associated Equipment*, vol. 601, no. 3, pp. 294–316, 2009.
- 443 [6] Hamamatsu, “Datasheet,” URL: <https://www.hamamatsu.com/>, 2018.
- 444 [7] R. Abbasi, Y. Abdou, T. Abu-Zayyad, J. Adams, J. Aguilar, M. Ahlers, K. Andeen, J. Auffenberg,  
445 X. Bai, M. Baker, *et al.*, “Calibration and characterization of the icecube photomultiplier tube,”  
446 *Nuclear Instruments and Methods in Physics Research Section A: Accelerators, Spectrometers,*  
447 *Detectors and Associated Equipment*, vol. 618, no. 1-3, pp. 139–152, 2010.
- 448 [8] M. Aartsen *et al.*, “The icecube neutrino observatory: Instrumentation and online systems, jinst 12  
449 (03)(2017) p03012,” *arXiv preprint arXiv:1612.05093*, pp. 1748–0221.
- 450 [9] R. Stokstad, “Design and performance of the icecube electronics,” 2005.
- 451 [10] Hamamatsu, “Resources: Basics and applications,” URL:  
452 [https://www.hamamatsu.com/resources/pdf/etd/PMT\\_handbook\\_v3aE.pdf](https://www.hamamatsu.com/resources/pdf/etd/PMT_handbook_v3aE.pdf), 2018.
- 453 [11] Hamamatsu, “Handbook resources, chapter 4,” URL:  
454 [https://www.hamamatsu.com/resources/pdf/etd/PMT\\_handbook\\_v3aE-Chapter4.pdf](https://www.hamamatsu.com/resources/pdf/etd/PMT_handbook_v3aE-Chapter4.pdf), 2018.
- 455 [12] J. Brack, B. Delgado, J. Dhooghe, J. Felde, B. Gookin, S. Grullon, J. Klein, R. Knapik, A. LaTorre,  
456 S. Seibert, *et al.*, “Characterization of the hamamatsu r11780 12 in. photomultiplier tube,” *Nuclear*  
457 *Instruments and Methods in Physics Research Section A: Accelerators, Spectrometers, Detectors and*  
458 *Associated Equipment*, vol. 712, pp. 162–173, 2013.
- 459 [13] E. Calvo, M. Cerrada, C. Fernández-Bedoya, I. Gil-Botella, C. Palomares, I. Rodríguez, F. Toral, and  
460 A. Verdugo, “Characterization of large-area photomultipliers under low magnetic fields: Design and  
461 performance of the magnetic shielding for the double chooz neutrino experiment,” *Nuclear*  
462 *Instruments and Methods in Physics Research Section A: Accelerators, Spectrometers, Detectors and*  
463 *Associated Equipment*, vol. 621, no. 1-3, pp. 222–230, 2010.
- 464 [14] F. Kaether and C. Langbrandtner, “Transit time and charge correlations of single photoelectron events  
465 in r7081 photomultiplier tubes,” *Journal of Instrumentation*, vol. 7, no. 09, p. P09002, 2012.
- 466 [15] B. Lubsandorzhev, P. Pokhil, R. Vasiljev, and A. Wright, “Studies of prepulses and late pulses in the  
467 8" electron tubes series of photomultipliers,” *Nuclear Instruments and Methods in Physics Research*  
468 *Section A: Accelerators, Spectrometers, Detectors and Associated Equipment*, vol. 442, no. 1-3,  
469 pp. 452–458, 2000.

- 470 [16] K. Ma, W. Kang, J. Ahn, S. Choi, Y. Choi, M. Hwang, J. Jang, E. Jeon, K. Joo, H. Kim, *et al.*, “Time  
471 and amplitude of afterpulse measured with a large size photomultiplier tube,” *Nuclear Instruments*  
472 *and Methods in Physics Research Section A: Accelerators, Spectrometers, Detectors and Associated*  
473 *Equipment*, vol. 629, no. 1, pp. 93–100, 2011.
- 474 [17] S. Torre, T. Antonioli, and P. Benetti, “Study of afterpulse effects in photomultipliers,” *Review of*  
475 *scientific instruments*, vol. 54, no. 12, pp. 1777–1780, 1983.
- 476 [18] M. Aartsen, K. Abraham, M. Ackermann, J. Adams, J. Aguilar, M. Ahlers, M. Ahrens, D. Altmann,  
477 T. Anderson, M. Archinger, *et al.*, “Characterization of the atmospheric muon flux in icecube,”  
478 *Astroparticle physics*, vol. 78, pp. 1–27, 2016.
- 479 [19] M. Aartsen, R. Abbasi, Y. Abdou, M. Ackermann, J. Adams, J. Aguilar, M. Ahlers, D. Altmann,  
480 J. Auffenberg, X. Bai, *et al.*, “Measurement of south pole ice transparency with the icecube led  
481 calibration system,” *Nuclear Instruments and Methods in Physics Research Section A: Accelerators,*  
482 *Spectrometers, Detectors and Associated Equipment*, vol. 711, pp. 73–89, 2013.
- 483 [20] R. Dossi, A. Ianni, G. Ranucci, and O. J. Smirnov, “Methods for precise photoelectron counting with  
484 photomultipliers,” *Nuclear Instruments and Methods in Physics Research Section A: Accelerators,*  
485 *Spectrometers, Detectors and Associated Equipment*, vol. 451, no. 3, pp. 623–637, 2000.